

# Compressible Separator and Catalyst for Simultaneous Separation and Purification of Emulsions and Aqueous Pollutants

Hee Ju Kim, Young Ju Jung, Su Hyeon Son, and Won San Choi\*

Cite This: *ACS Omega* 2023, 8, 40741–40753

Read Online

ACCESS |



Metrics &amp; More

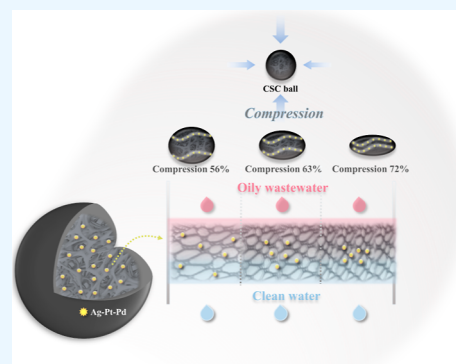


Article Recommendations



Supporting Information

**ABSTRACT:** Oily wastewater, a global environmental concern, demands efficient oil/water separation and pollutant removal. Our compressible separator and catalyst (CSC) balls, prepared through sponge etching and metal nanoparticle synthesis, exhibited efficient degradation of dyes of varying sizes, spanning a molecular weight range from 139 to 696 g/mol during the oil/water separation. Control over the distance between catalysts was achieved by incorporating Ag–Pt–Pd catalysts into the sponge skeleton and by adjusting the compression rates. The dispersion of the catalysts improved degradation efficiency for larger dyes, while concentrating the catalysts proved to be more effective for the smaller ones. By optimizing the compression rates of CSC balls, we successfully achieved the effective removal of emulsions of different sizes and precise control of flux. Our CSC ball-loaded system offers efficient and versatile solutions for concurrent separation and purification of emulsions and pollutants with potential environmental benefits.



## 1. INTRODUCTION

Oily wastewater poses a significant environmental challenge in both developing and developed countries due to its detrimental impact on human health and ecosystems. Due to the industry's advancement, there has been a simultaneous increase in both the volume and variety of constituent materials present in the emission of oily wastewater. Oily wastewater, a type of industrial wastewater, often contains hazardous aqueous pollutants.<sup>1,2</sup> Prior to discharge, it is necessary to separate the oil/water mixture and remove the aqueous pollutants from the water. While numerous studies have been conducted on oil/water separation,<sup>3–15</sup> only a limited number of researchers have focused on exploring materials and technologies that possess the ability to simultaneously achieve both oil/water separation and pollutant purification.<sup>16–19</sup> Two approaches, namely, the filter type and particle type, have been proposed for the removal of aqueous pollutants during oil/water separation. In the filter-type approach, the oil/water mixture is first separated, followed by the decomposition of organic matter in the water using a catalyst.<sup>16–18</sup> On the other hand, in the particle-type approach, the organic matter is decomposed using a particle catalyst, and then the oil/water mixture is separated using particles.<sup>19</sup> The filter-type approach suffers from drawbacks, such as long processing time and challenges in emulsion separation. Conversely, the particle-type approach carries the risk of particle outflow and exhibits a lower separation capacity. Consequently, it is essential to develop novel processing technologies and materials that can accentuate two benefits while compensating for their limitations.

An oil/water mixture can be categorized into two types: immiscible oil/water mixture and emulsified oil/water mixture, which includes oil-in-water (O/W) or water-in-oil (W/O) emulsions.<sup>20</sup> The separation of the immiscible oil/water mixture is relatively straightforward due to the density difference between the two phases. However, the presence of an emulsified oil/water mixture poses a greater challenge in separation due to its stable dispersion within the immiscible continuous phase. Moreover, the difficulty of separation is further amplified when dealing with small-sized emulsions that are smaller than 20  $\mu\text{m}$ .<sup>21</sup> Various methods, such as solvent extraction, irradiation, oxidation, microwaves, and landfill, have been employed to address the challenge of emulsion separation. However, these methods often suffer from low efficiency and high costs, limiting their applicability. In contrast, membrane-based filtration technologies have emerged as a promising solution, offering high separation efficiency, low energy costs, environmental friendliness, and excellent selectivity.<sup>20</sup> The key to successful emulsion separation lies in filtration membranes, which leverage special wettability and size-based effects.<sup>22,23</sup> Membrane materials can be derived from common substrates such as polymers, carbon, ceramic, metal meshes, gel, and biomass.<sup>24–29</sup> For instance, the Tseng

Received: August 7, 2023

Revised: September 25, 2023

Accepted: October 10, 2023

Published: October 20, 2023



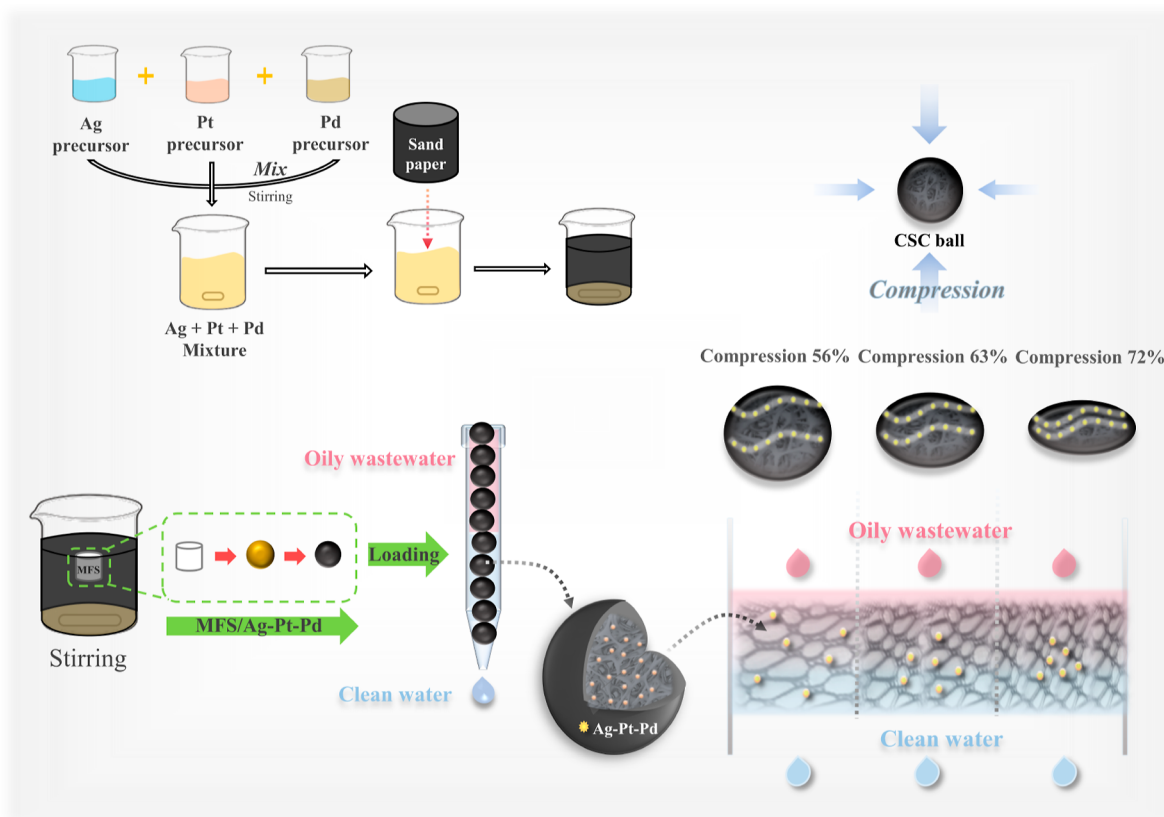


**Figure 1.** Schematic illustration of CSC ball formation and a novel column filtration system utilizing loaded CSC balls for the simultaneous removal of emulsions and aqueous pollutants.

group introduced superoleophilic and superhydrophobic carbon membranes designed for efficient separation of trace water-in-oil emulsions.<sup>25</sup> In another study, Hou's group developed nanofiber membranes utilizing natural loofah and poly(vinylidene fluoride) (PVDF) for gravity-driven water purification.<sup>29</sup> More recently, the Xie group synthesized coaxial electrospun nanofibrous aerogel membranes, effectively facilitating oil removal and water-in-oil emulsion separation.<sup>28</sup> These materials enable the development of convenient and effective membranes for emulsion purification. However, a major challenge lies in achieving high flux rates for these membranes with pore sizes ranging from several tens of nanometers to hundreds of nanometers. A diverse array of flux control techniques is also essential, as the flux requirements fluctuate across different application fields.

In this letter, we present a novel compressible separator and catalyst (CSC) ball-loaded column system. This system utilizes tightly packed spherical CSC balls to effectively separate emulsions and decompose pollutants. The CSC balls exhibit the ability to rapidly separate O/W emulsions while achieving a high flux and decomposition efficiency for aqueous pollutants. By adjusting the compression rates of the catalyst-coated sponge, it becomes possible to control the distance between the catalysts and the pore size within the porous and flexible CSC ball.

## 2. EXPERIMENTAL SECTION

**2.1. Materials.** A sulfate melamine formaldehyde sponge (MFS) was purchased from BASF. Silver nitrate ( $\text{AgNO}_3$ ,  $\geq 99.0\%$ ), chloroplatinic acid hydrate ( $\text{H}_2\text{Cl}_6\text{Pt}\cdot\text{H}_2\text{O}$ ,  $\geq 99.9\%$ ), palladium(II) nitrate hydrate ( $\text{Pd}(\text{NO}_3)_2\cdot\text{H}_2\text{O}$ ), sodium

borohydride ( $\text{NaBH}_4$ , 98%), span 80 ( $M_w$ : 428.6  $\text{g mol}^{-1}$  and  $d$ : 0.986  $\text{g mL}^{-1}$ ), methyl orange (MO), methylene blue (MB), Congo red (CR), rhodamine 6G (R6G), and 4-nitrophenol (4-NP) were purchased from Sigma-Aldrich. Soybean oil was purchased from CJ (Korea). All chemicals were used without further purification. Deionized (DI) water with a resistance of 18  $\text{M}\Omega\cdot\text{cm}$  was obtained from a Millipore Simplicity 185 system.

**2.2. Preparation of CSC-18 Balls.** CSC-18 balls (MFS/Ag–Pt–Pd NP) were prepared by immersing 20 cylindrical MFS pieces ( $D$ : 10 mm and  $H$ : 10 mm) into a sandpaper-wrapped beaker containing a mixed metal precursor solution (300 mL) composed of silver nitrate (0.1 g), chloroplatinic acid hydrate (0.1 g), and palladium nitrate hydrate (0.07 g). The solution was vigorously stirred at room temperature for 6 h. The resulting CSC balls were washed three times with DI water and then reduced with a 5 mM  $\text{NaBH}_4$  solution for 30 min. Finally, the CSC balls (MFS/Ag–Pt–Pd NP) were washed three times with DI water and dried at 50 °C for 12 h.

**2.3. Catalytic Test for Reductive Degradation of Dyes.** To conduct the catalytic test for the reductive degradation of dyes, the following procedure was followed. First, 15 mL of each dye solution (0.08 mM) and 7 mL of  $\text{NaBH}_4$  solution (100 mM) were freshly prepared. These two solutions were then combined, resulting in a mixed solution. Next, the mixed solution was poured into a catalysis column system loaded with CSC balls. Afterward, 2 mL of the filtered solution was extracted from the system and subjected to analysis by using UV–vis spectroscopy.

**2.4. O/W Emulsion Separation.** To prepare an O/W emulsion, soybean oil (2 mL), span 80 (0.03 g), and water (99

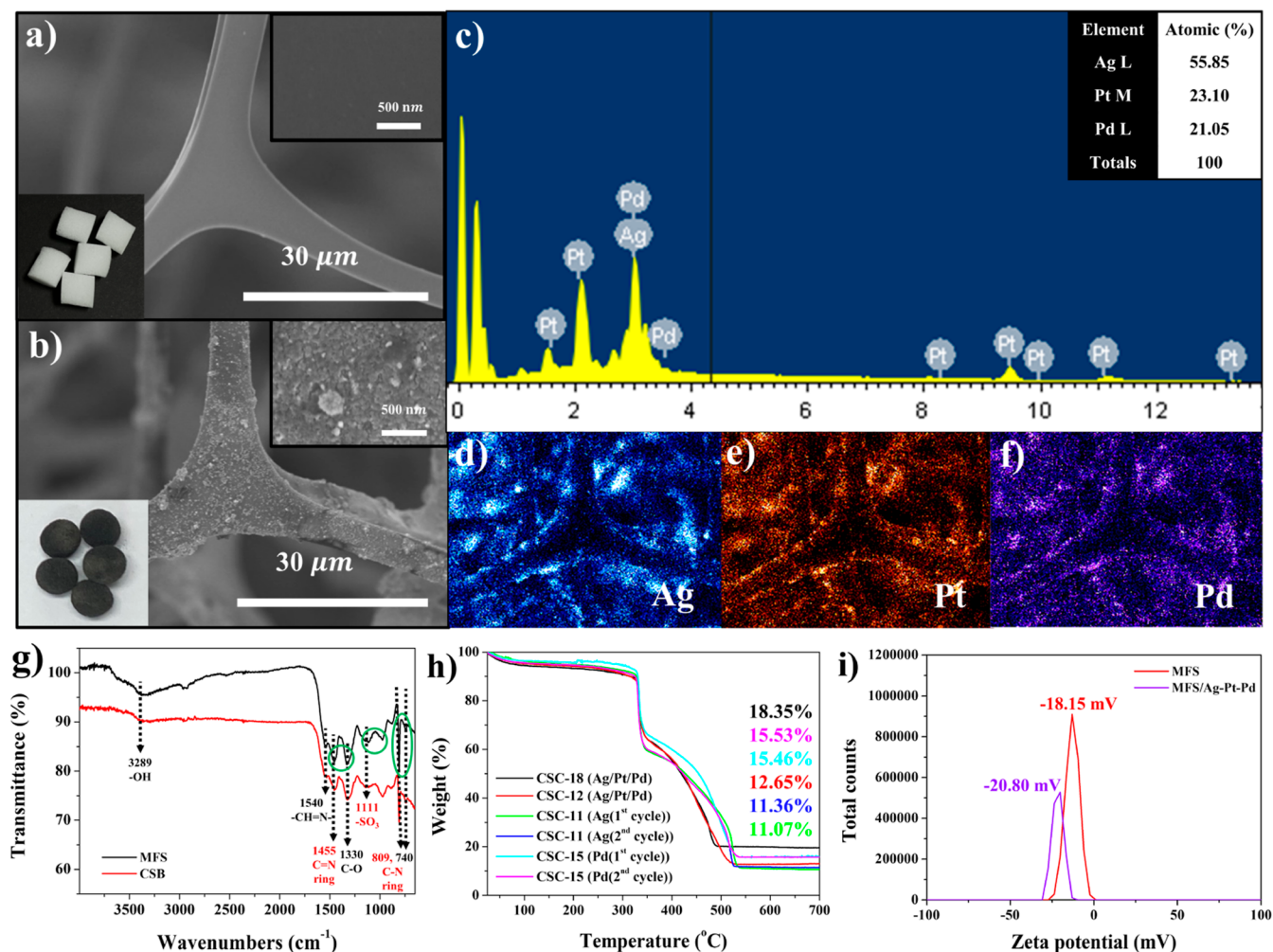


**Figure 2.** (a,b) SEM images of the MFS and CSC ball (MFS/Ag–Pt–Pd). The insets display the images of the cylindrical MFS and the CSC ball (MFS/Ag–Pt–Pd). (c) EDX and (d–f) mapping data of the CSC ball (MFS/Ag–Pt–Pd). (g) FT-IR data of the MFS and CSC ball (MFS/Ag–Pt–Pd). (h) TGA data of the CSC ball (MFS/Ag–Pt–Pd), CSC ball (MFS/Ag), and CSC ball (MFS/Pd). (i) Zeta potential data of the MFS and CSC ball (MFS/Ag–Pt–Pd).

mL) were mixed together and stirred for 1 h at T15% and 2 h at T5%. Next, 6 mL of the prepared emulsion was poured into a column system loaded with CSC balls. The emulsion was then subjected to filtration, and 2 mL of the filtered solution was extracted from the system for further analysis by using UV–vis spectroscopy.

**2.5. Characterization.** Scanning electron microscopy (SEM)/energy-dispersive X-ray (EDX) analyses were performed by using a Hitachi S-4800 instrument. Thermogravimetric analysis (TGA) was performed using a thermogravimetric analyzer (Sinco TGA N-1500) over a temperature range of 25–800 °C at a heating rate of 5 °C min<sup>-1</sup> in air (flow rate, 60 cm<sup>2</sup>/min). UV–vis absorption spectra were recorded on a UV–vis spectrophotometer (Sinco Evolution 201). FT-IR spectra were obtained by using a Sinco Nicolet ISS instrument. Optical microscopy measurements were performed on a Leica DM IL LED instrument after a drop of an emulsion solution was placed on a microscope slide glass. The zeta potential measurements were performed on a Malvern Nano-ZS Zetasizer at room temperature. By comparing the volumes before and after compression, the compression rate can be calculated according to the following equation

$$\text{Compression rate (\%)} = (V_i - V_f) / V_i \times 100\%$$

where  $V_i$  (mm<sup>3</sup>) and  $V_f$  (mm<sup>3</sup>) refer to the volumes before and after compression, respectively. The volume of a catalysis column was premeasured and marked with a scale. Subsequently, the CSC ball was inserted into the column, and a specific weight was placed on top of it. After a designated period, the weight was removed, and the volume of the CSC ball was measured and recorded to correspond with each scale marking. In order to create three sets, each consisting of 6 CSC-18 balls compressed to 56, 63, and 72%, the procedure involved loading six CSC-18 balls into conical cylinders. Subsequently, weights of 50, 100, and 200 g were positioned on top of the corresponding set of six CSC-18 balls for a duration of 5 min. To ensure the uniformity of column manufacturing, CSC balls with an average size were consistently chosen for each experiment. Furthermore, columns with an average compression ratio were selected and tested, even after the CSC balls were loaded into the column.

### 3. RESULTS AND DISCUSSION

**3.1. Synthesis of CSC Balls.** Figure 1 shows a schematic illustration of the formation of a CSC ball through physical

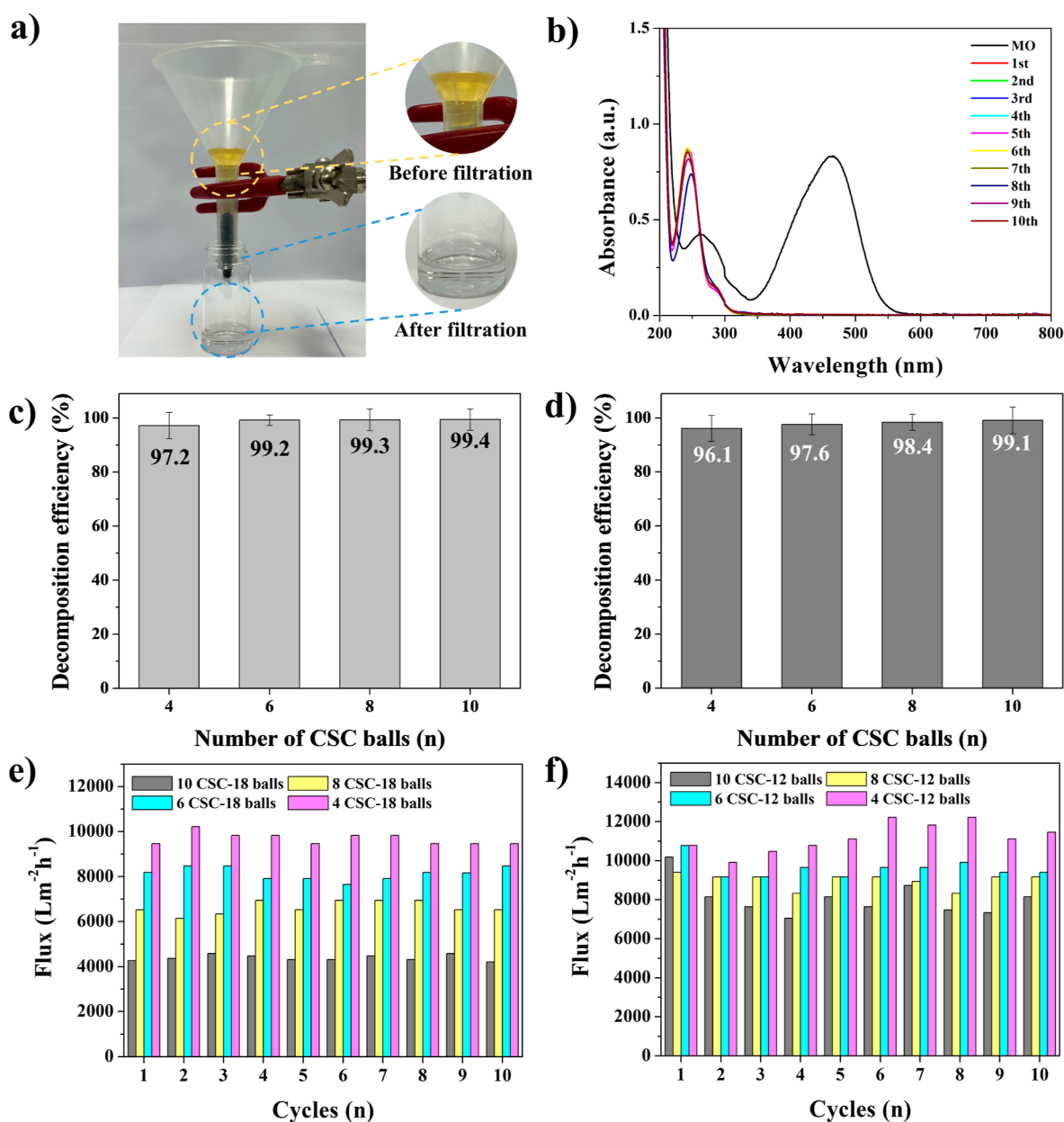


**Figure 3.** (a) Catalytic test setup of the column filtration system loaded with CSC balls. (b) UV–vis absorption spectral changes in the decomposition of MO catalyzed by 10 CSC-18 balls. Reuse tests for MO until the 10th cycle. (c) Decomposition efficiency of MO catalyzed by 10, 8, 6, and 4 CSC-18 balls. (d) Decomposition efficiency of MO catalyzed by 10, 8, 6, and 4 CSC-12 balls. (e) Flux capacity of MO filtration using 10, 8, 6, and 4 CSC-18 balls. (f) Flux capacity of MO filtration using 10, 8, 6, and 4 CSC-12 balls.

etching of a melamine formaldehyde sponge (MFS), followed by the synthesis of noble metal nanoparticles (NPs). The MFS is chosen as the base material due to its compressible, porous, and sulfonated functional properties. The CSC ball (MFS/Ag–Pt–Pd NP) is prepared by the immersion of the cylindrical MFS into a beaker wrapped in sandpaper, which contains the mixed metal precursor solution. During the stirring of the resulting solution, the cylindrical MFS with a centimeter scale is gradually transformed into a tiny spherical MFS by the collision between the MFS and sandpaper. During physical etching, three types of metal precursors are simultaneously adsorbed onto the sulfonated groups of the MFS for the synthesis of noble metal NPs. After reduction treatment, three types of metal NP-loaded CSC balls are formed. A conical cylinder filled with 1–10 CSC balls can be

used to simultaneously separate and purify O/W emulsions and aqueous pollutants, respectively.

**3.2. Characterization of CSC Balls.** Figure 2a,b shows the SEM images of the MFS and CSC ball (MFS/Ag–Pt–Pd NP). The MFS exhibited a smooth surface with a three-dimensional network structure, while the CSC ball displayed a rough surface composed of both large (average 310 nm) and small (average 40 nm) particles, indicating successful synthesis of metal NPs on the MFS. The surface of the CSC ball revealed the presence of particles smaller and larger than 100 nm, which were identified as three types of metal NPs and complexes composed of three types of precursors, respectively (inset of Figure 2b). The MFS is characterized by its cylindrical shape, white color, and an average size of 10 mm, whereas the CSC ball is characterized by its spherical shape, black color, and

average size of 9 nm (insets of Figure 2a,b). The synthesis of Ag, Pt, and Pd metal NPs on the MFS was confirmed through EDX and mapping data, which provided information about the presence and content of each metal species (Figure 2c–f). The highest content was observed in Ag, with Pt and Pd showing a similar content ( $\text{Ag} > \text{Pt} \approx \text{Pd}$ ; Figure 2c). The mapping data confirm the presence of three types of elements (Ag, Pt, and Pd) (Figure 2d–f). To further confirm the synthesis of the three types of NPs on MFS, FT-IR spectroscopy was conducted. The peak intensities at  $1455\text{ cm}^{-1}$  (C=N stretching),  $1111\text{ cm}^{-1}$  ( $-\text{SO}_3^-$  stretching), and  $809\text{ cm}^{-1}$  (C–N stretching) were observed to decrease in the CSC sample compared to the corresponding peaks in the pristine MFS samples (red line, Figure 2g). This observation suggests that a reaction took place between groups possessing unshared electron (N) pairs (or  $-\text{SO}_3^-$ ) and metal precursors. The TGA data showed that the CSC ball (MFS/Ag–Pt–Pd NP) had an inorganic portion of 12–18% (red and black lines, Figure 2h), indicating the presence of 12–18% metal NPs. To investigate the possibility of controlling the metal content within the CSC ball, single metals or mixed metals were synthesized. By variation of the reaction cycle, the content of metal NPs within the CSC ball could be controlled for the synthesis of the three types of mixed metals (Ag, Pt, and Pd). The metal content within the CSC ball measured in the first cycle was 12%, which increased to 18% in the second cycle (red and black lines, Figure 2h). However, the metal contents in the CSC ball were limited to approximately 11 and 15% for single metal (Ag and Pd), respectively, and did not increase even though the reaction cycle increased (green/blue and ice blue/pink lines, Figure 2h). These values are estimated to be the maximum content of Ag and Pd that can be synthesized in the CSC ball. However, in the case of three types of metals, a higher content was obtained because cation (Ag and Pd) and anion (Pt) precursors were mixed, allowing them to be coated on MFS while forming complexes. Thus, as shown in Figure 2b, it is estimated that large particles consist of complexes composed of metal NPs, while small particles consist of individual metal NPs. The results suggest that three types of metal NPs with higher content can be synthesized in the CSC balls by using a mixed metal system with oppositely charged precursors. Due to the high pH of the Pt precursor solution, the MFS was oxidized, which made the synthesis of Pt NPs alone impossible. The zeta potential of the CSC ball (MFS/Ag–Pt–Pd) was found to be  $-20.8\text{ mV}$ , which was slightly lower compared to that of MFS ( $-18.2\text{ mV}$ ) (Figure 2i). These findings suggest that the CSC ball (MFS/Ag–Pt–Pd) still maintains a negatively charged surface, even after the synthesis of three types of metal NPs on the surface of MFS. A water droplet was rapidly absorbed by the CSC ball sample (Figure S1). The water contact angle (WCA) measured on the CSC ball sample was  $0^\circ$ , indicative of its superhydrophilic nature (Figure S1).

**3.3. Catalytic Activity and Flux of CSC Balls.** To evaluate the catalytic activity of the CSC balls, a catalysis column system was employed. Specifically, 4–10 CSC balls were loaded into a conical cylinder with a volume of 2 mL and used to purify aqueous pollutants (Figure 3a). The CSC balls with metal contents of 12 and 18% were labeled CSC-12 and CSC-18, respectively. Five types of dyes including MO, MB, CR, R6G, and 4-NP were selected based on their known harmful effects on human health and the environment. The selection of these dyes also took into consideration the type of

charge and size of each molecule. The 10 CSC balls with the highest number were tested first. After the 10 CSC-18 balls were pretreated with water, the MO solution rapidly penetrated the 10 CSC-18 balls when the MO solution was poured into a conical cylinder loaded with the 10 CSC-18 balls (Figure 3a). A transparent solution was obtained that could not be distinguished by the naked eye. Figure 3b shows the UV–vis spectra of MO degradation catalyzed by the 10 CSC-18 balls. After a single filtration, the absorption peak of MO at 460 nm decreased and stabilized, accompanied by the emergence of a new peak at around 250 nm, indicating the degradation of MO. The appearance of the new peak can be attributed to the cleavage of the azo bond ( $-\text{N}=\text{N}-$ ) in MO, which contains an azo-benzene group that absorbs at 460 nm.<sup>30,31</sup> This process leads to the generation of new degradation products. It is believed that possible degradation products include sulfanilic acid and *N,N*-dimethyl-*p*-phenylenediamine, which have UV absorption at a wavelength of 240–250 nm.<sup>30,31</sup>

To investigate the effect of the number of CSC-18 balls on their catalytic activity, experiments were conducted using 10, 8, 6, and 4 balls. The results showed that the 10, 8, and 6 CSC-18 balls exhibited similar decomposition efficiencies (DEs) of 99.4, 99.3, and 99.2%, respectively, which were all higher than the DE obtained using 4 CSC-18 balls (97.2%) (Figure 3c). The results suggest that using only four CSC-18 balls was not enough to decompose most of the MO in one filtration, whereas using more than six balls was sufficient to achieve this. Comparative experiments were conducted using 10, 8, 6, and 4 CSC-12 balls to investigate the effect of the metal content on the catalytic activity of the CSC balls. The CSC-12 ball has metal contents lower than those of the CSC-18 balls. The DEs of CSC-12 balls gradually increased as the number of balls increased, suggesting that the catalytic activity of the catalysis column system can be controlled by varying the number of CSC-12 balls used (Figure 3d). The DE of 10 CSC-12 balls was 99.1%, which was similar to the DEs observed for 10, 8, and 6 CSC-18 balls. These results indicate that for the decomposition of MO, an increase in the number of CSC-12 balls is required when using CSC-12, whereas a small number of CSC-18 balls is sufficient when using CSC-18. When evaluating the effectiveness of filters, it is crucial to consider the flux factor as one of the key components. MO solution was used to investigate the fluxes of CSC-12 and CSC-18. As the number of CSC balls decreases, the flux increases (Mocha → yellow → ice blue → pink bars, Figure 3e,f). This inverse relationship holds true in both cases (Figure 3e,f). The CSC-18 balls with 10, 8, 6, and 4 counts exhibited lower flux rates compared to the CSC-12 balls with the same counts due to their higher metal content. However, the 10, 8, and 6 CSC-18 balls demonstrated relatively high average flux rates of 4390, 6637, and 8135 L/m<sup>2</sup> h, respectively (Figure 3e). Additionally, based on the data presented in Figure 3c, it can be observed that the 10, 8, and 6 CSC-18 balls exhibited comparable DEs, ranging from 99.4 to 99.2%. Therefore, in some circumstances, using only 6 CSC-18 balls with a high flux rate of 8135 L/m<sup>2</sup> h and a DE of 99.2% may be a practical substitute for using 10 CSC-18 balls. Thus, considering the high flux and DE of 6 CSC-18 balls, the 6 CSC-18 balls were determined to be an optimized condition for a catalysis column system.

**3.4. Effect of Size and Charge of Pollutants on the Decomposition Efficiency of CSC Balls.** To examine the impact of the size and charge of aqueous pollutants on the DE of CSC-18 balls, we conducted tests using MB, 4-NP, CR, and

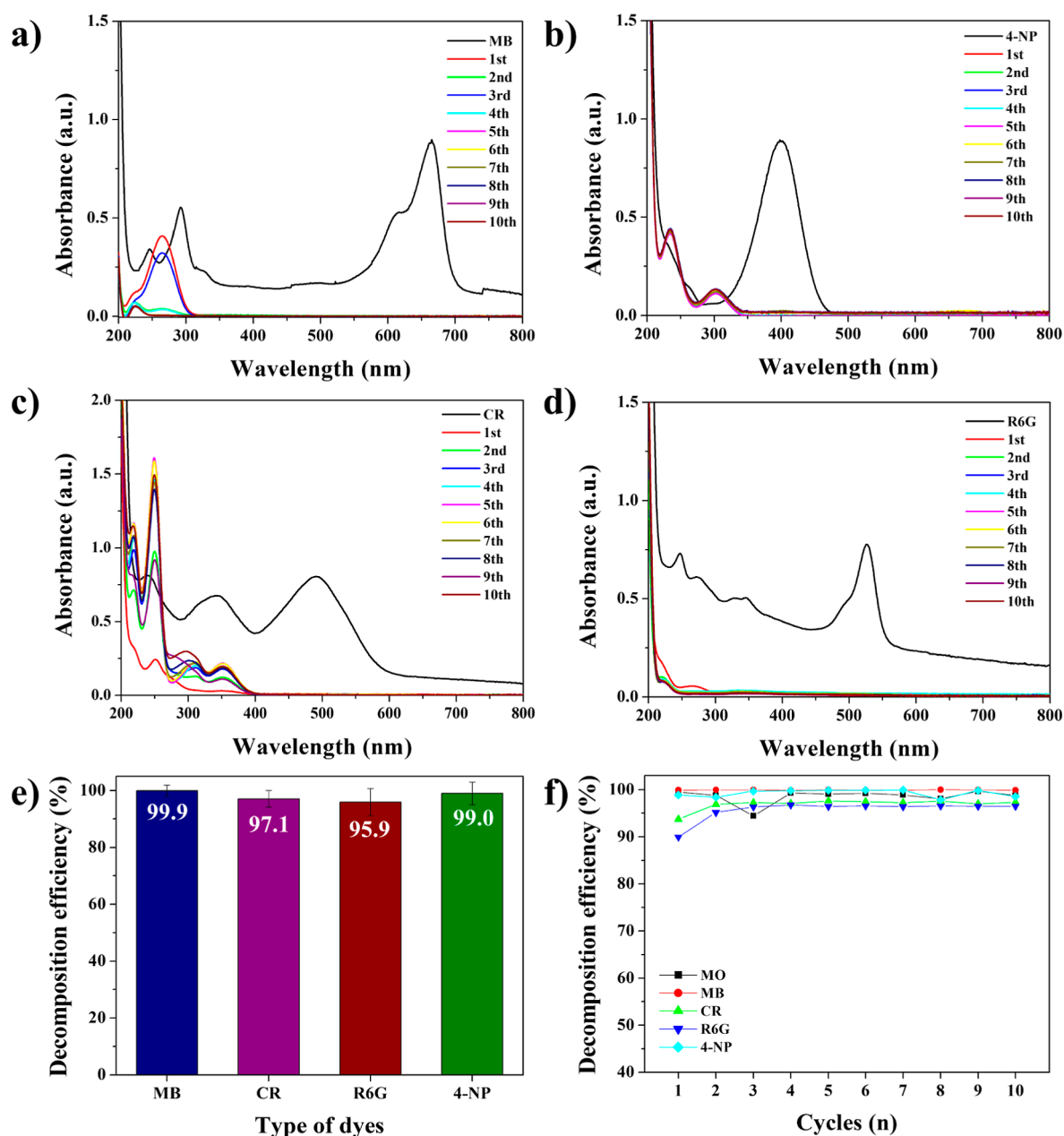


**Figure 4.** UV-vis absorption spectral changes in the decomposition of (a) MB, (b) 4-NP, (c) CR, and (d) R6G catalyzed by 6 CSC-18 balls. Reuse tests for each dye up to the 10th cycle. (e) Average decomposition efficiency and (f) efficiency variation of each dye catalyzed by 6 CSC-18 balls until the 10th cycle.

R6G. The 6 CSC-18 balls showed high DEs of 99.9 and 99% for MB and 4-NP, respectively, which were comparable with that of MO (99.2%) (Figures 4a,b,e, and 3c). The charge of pollutants did not have a significant impact on the DE of the 6 CSC-18 balls, as the negatively charged 6 CSC-18 balls demonstrated similar DEs for MO (−), MB (+), and 4-NP (−) (Figures 4a,b,e, and 3c). The DE of the pollutants was more significantly influenced by their sizes than their charges. The 6 CSC-18 balls demonstrated DEs of 97.1 and 95.9% for CR (−) and R6G (+), respectively, which have large molecular sizes. These DEs were lower compared to those achieved for MO (99.2%), MB (99.9%), and 4-NP (99%), which have smaller molecular sizes. The 6 CSC-18 balls showed the highest DE for MB [MB (+) > MO (−) > 4-NP (−) > CR (−) > R6G (+)], indicating that the CSC was more effective at

breaking down small-sized dyes like MB, MO, and 4-NP, regardless of the charge of the pollutant. The results mentioned above were obtained by a filtration method using 6 CSC-18 balls for 10 cycles. Despite the repeated use of the 6 CSC-18 balls, there was no significant change in the DE observed, indicating that the filtration treatment using 6 CSC-18 balls could be utilized for long-term use (Figure 4f). In order to investigate the potential leakage of metal NPs from the CSC-18 balls, six newly acquired CSC-18 balls were carefully inserted into conical cylinders. Subsequently, deionized water was allowed to pass through these cylinders for a total of 10 cycles.

Notably, the conducted tests did not reveal any discernible characteristic peaks corresponding to the three types of metal NPs (Figure S2). A plausible mechanism underlying the

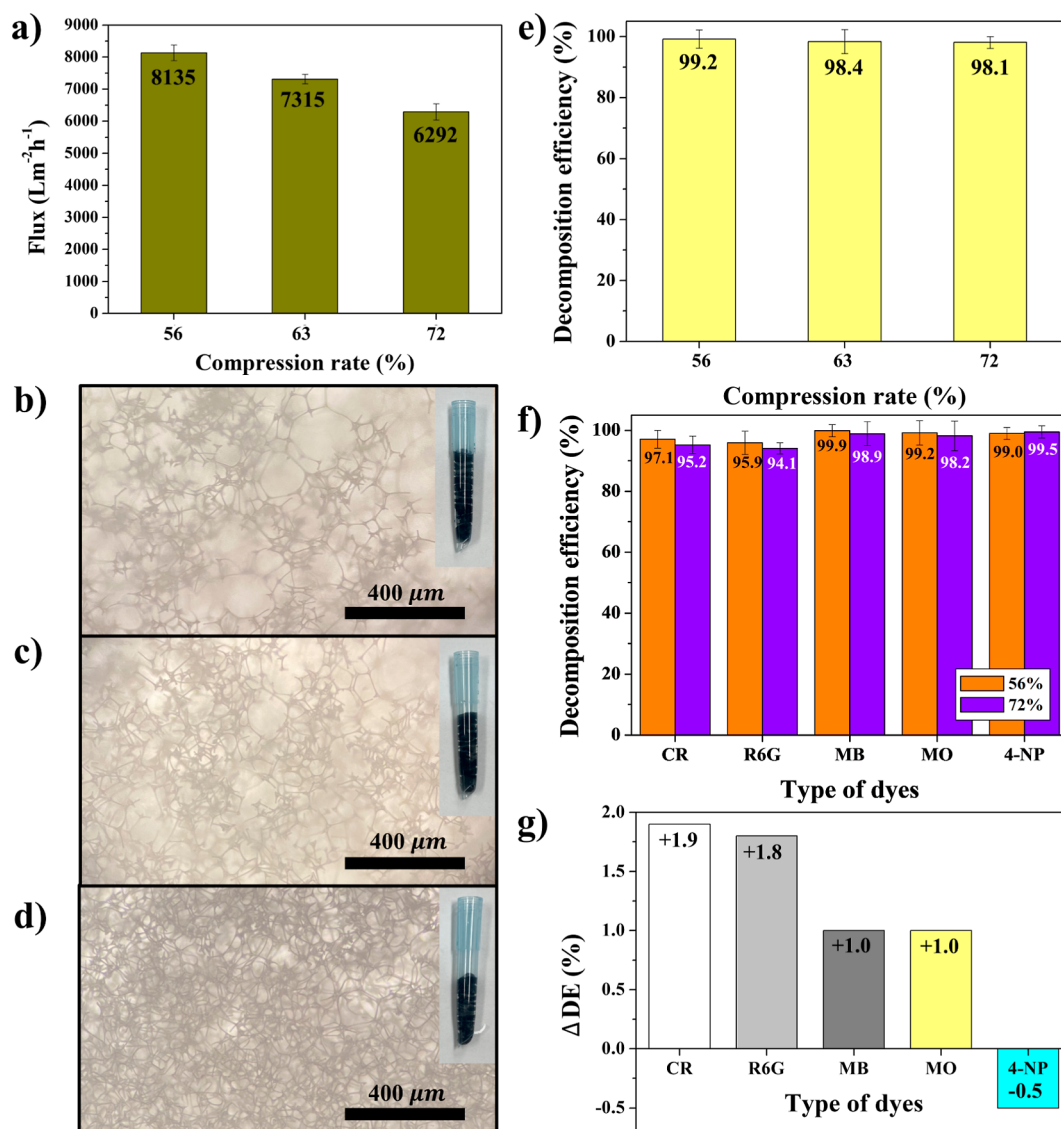


**Figure 5.** (a) Flux capacity and (b–d) optical microscopy images of six CSC-18 balls at compression rates of 56, 63, and 72%. Insets display conical cylinders loaded with six CSC-18 balls at different compression rates. (e) Decomposition efficiency of MO catalyzed by six CSC-18 balls with compression rates of 56, 63, and 72%. (f) Decomposition efficiency and (g)  $\Delta\text{DE}$  of MO, MB, CR, R6G, and 4-NP catalyzed by six CSC-18 balls at compression rates of 56 and 72%. These results demonstrated an inverse relationship between the compression rate and flux. The catalytic activity of six CSC-18 balls with different compression rates was tested. Among them, those with compression rates of 56, 63, and 72% showed DEs of 99.2, 98.4, and 98.1%, respectively, for the degradation of MO (e). Although it was expected that the six CSC-18 balls with the highest compression rate would exhibit the highest DE due to their low flux (or high retention time), the results were the opposite. The six CSC-18 balls with the lowest compression rate, indicating the longest distance between the catalysts, exhibited the highest efficiency. The synthesis of Ag–Pt–Pd catalysts in the sponge ball's skeleton enables the control of the distance between the catalysts by adjusting the compression rates of the sponge. In other words, the compression rate of 56% resulted in higher DEs compared to the compression rate of 72%, indicating that dispersing the catalysts yielded better results than concentrating them for the degradation of MO. This phenomenon was observed not only in MO but also in experiments involving other dyes. In most cases, the six CSC-18 balls with the compression rate of 56% exhibited higher DEs [orange bars, (f)]. This phenomenon was particularly noticeable for larger sized dyes ( $\Delta\text{DE} = 1.9, 1.8, 1, 1,$  and  $-0.5\%$  for CR, R6G, MB, MO, and 4-NP, respectively) (fg).

reduction of organic dyes, such as MO, CR, MB, and R6G, can be outlined as follows: The Au/Pt/Pd catalysts situated on the MFS serve as mediators for electron transfer throughout the catalytic process.<sup>32,33</sup>  $\text{BH}_4^-$  molecules promptly approach and contribute electrons to the surface of the Au/Pt/Pd catalyst located on the support. Subsequently, the Au/Pt/Pd catalysts residing on the MFS surface convey electrons to each dye molecule, prompting the reduction of each dye into compounds featuring a singular phenyl ring alongside an amine group. Notably, these transformed compounds exhibit considerably lower toxicity compared to the initial chem-

icals.<sup>32,33</sup> Utilizing Au catalysts for reductive decomposition, which represents an effective pretreatment method, yields cleavage of azo bonds within dye molecules. This transformative process results in the production of products that are more amenable to subsequent mineralization within biological treatment processes.<sup>34</sup>

**3.5. Effect of Compression on the Flux and Catalytic Activity of CSC Balls.** To investigate the effect of compression on the flux and catalytic activity of six CSC-18 balls, the balls were loaded into conical cylinders at three different compression rates. Three sets of six CSC-18 balls,

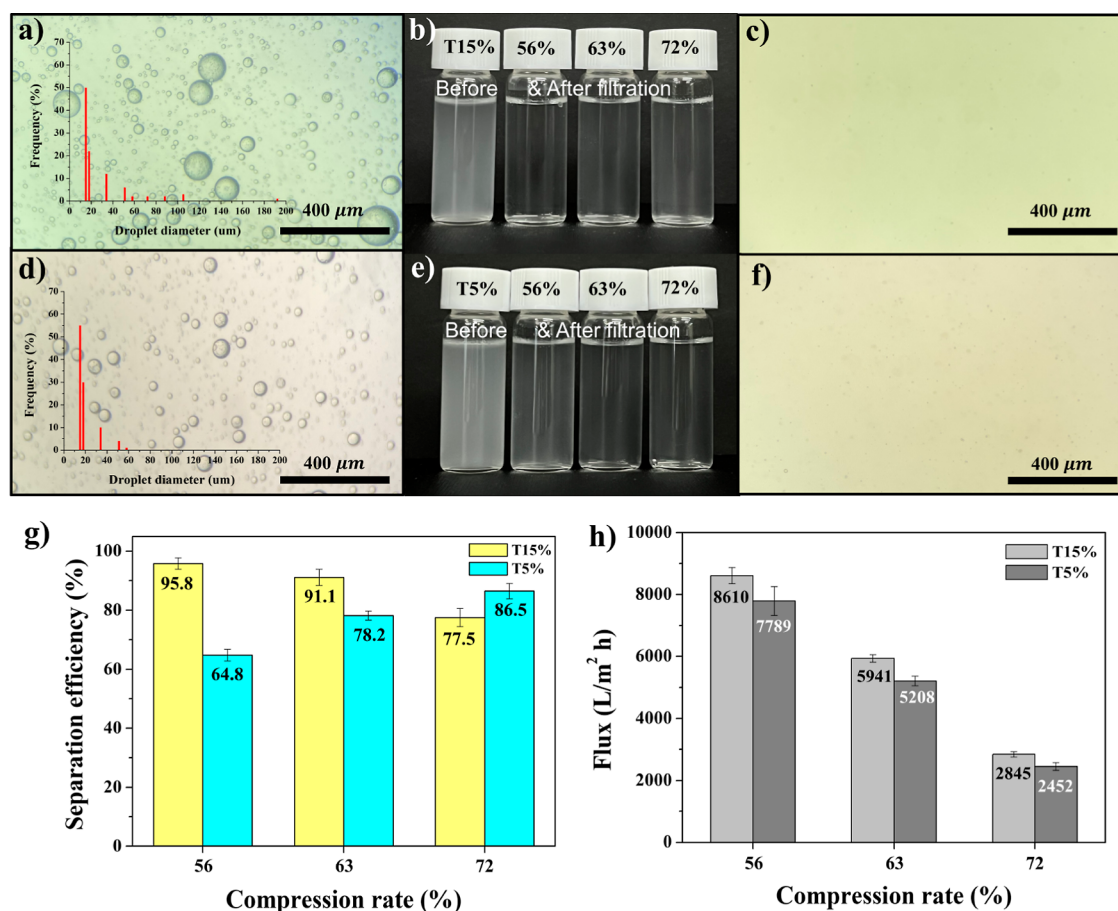


**Figure 6.** Optical microscopy images of the O/W emulsion (a,d) before and (c,f) after filtration by conical cylinders loaded with six CSC-18 balls at varying compression rates, with emulsion transmittances of (a–c) 15% and (d–f) 5%, respectively. Panels (b,e) display the corresponding images of the filtered solution. (g) Emulsion separation efficiencies and (h) flux capacities of the six CSC-18 balls at compression rates of 56, 63, and 72% for emulsions with transmittances of 15 and 5%.

compressed to 56, 63, and 72%, were tested for their flux and catalytic activity. The flux values of the six CSC-18 balls varied depending on the compression rate, with the highest and lowest fluxes observed in the balls compressed to 56 and 72%, respectively (Figure 5a). The six CSC-18 balls, which have compression rates of 56, 63, and 72%, exhibited pore sizes of 50–260, 41–152, and 32–85  $\mu\text{m}$ , respectively (Figure 5b–d). The corresponding flux values were 8135, 7315, and 6292  $\text{L}/\text{m}^2 \text{h}$ , respectively (Figure 5a). As the compression rate increased, the pore size decreased, leading to a lower flux (Figure 5a–d).

**3.6. Difference in Decomposition Efficiency between Compression Rates of CSC Balls.** The difference in DE between the compression rates was denoted as  $\Delta\text{DE}$  ( $\text{DE}_{56\%} - \text{DE}_{72\%}$ ). It means that as the  $\Delta\text{DE}$  value increases and becomes a larger positive value, it indicates that when the catalyst is dispersed, it is more efficient compared to when it is concentrated. Even after degradation, CR and R6G still have a relatively large molecular size (Figure S3). As a result, when these large-sized reactants and products are concentrated around the catalysts (the case of a compression rate of 72%), the transfer of the reactant to the catalysts is hindered. However, when the catalyst is dispersed (the case of the compression rate of 56%), catalytic reactions occur sequentially, which can help to alleviate overcrowding of reactants and products around the catalysts. Even in cases where the dye sizes were medium (MB and MB), this phenomenon was

observed (Figure 5g). As mentioned earlier, the diffusion of bulky dyes such as CR, R6G, MB, and MO toward the concentrated catalyst was hindered. However, even in the presence of 4-NP around the concentrated catalysts, the transfer of 4-NP to the catalysts was not hindered due to its significantly smaller size and its propensity for conversion rather than decomposition (Figure S3).

Thus, the  $\Delta\text{DE}$  value of 4-NP decreased and became a negative value, indicating that when the catalyst is concentrated (the compression rate of 72%), the retention time of 4-NP was extended, leading to increased catalyst efficiency compared to when it is dispersed (the compression rate of 56%) (Figure 5g). The above results indicate that dispersing the catalyst properly, rather than concentrating it in one location, and allowing the reactant to encounter and react with the catalyst sequentially can substantially enhance the efficiency of the catalyst for larger sized dyes. However, it has been observed that concentrating the catalyst yields higher efficiency, particularly for smaller sized dyes, compared to when it is dispersed. In other words, the determination of the distance between the catalysts is crucial for enhancing the DE. Thus, the determination of the optimal distance between catalysts should be based on the size of the dye. Our approach allows for precise control over the distance through the adjustment of the compression rates of the sponge.

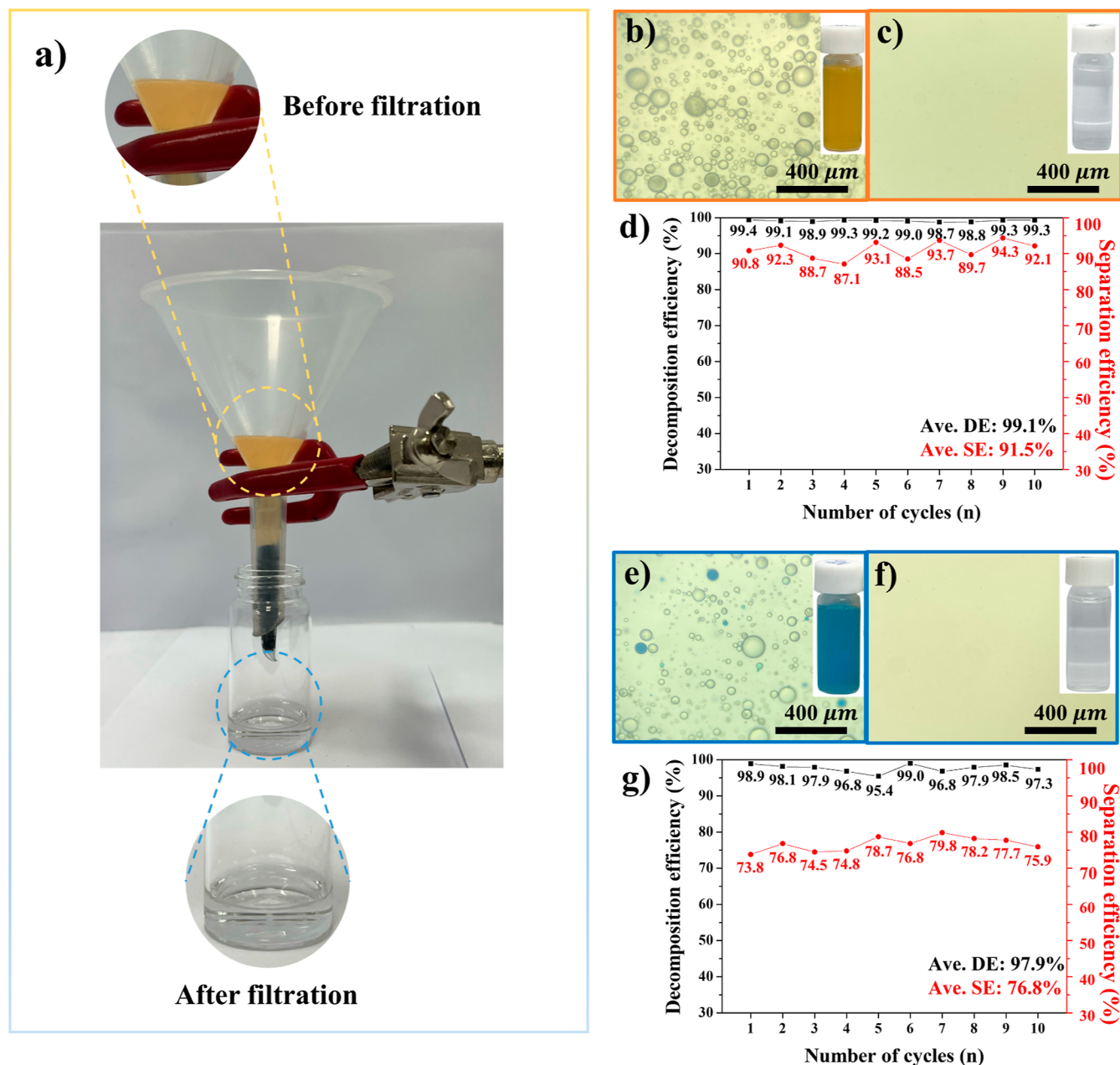
**3.7. Effect of Compression on the Separation Capability of CSC Balls.** To examine the impact of

Table 1. Performance Comparison of Polymer Membranes Reported in Previous Studies

material	permeation flux (L·m <sup>-2</sup> ·h <sup>-1</sup> )	separation efficiency (%)	type of emulsion	number of cycles	decomposition efficiency (%)	refs.
CSC-18	8135	95.8	O/W	10	99.1	our work
TiO <sub>2</sub> -fly ash/ $\alpha$ -Al <sub>2</sub> O <sub>3</sub>	668.34	98.7	O/W	3		13
Janus PAN	1410	99.8	O/W	10		14
SO@TDC/PM	55.3–118.6	91.3 $\pm$ 0.3	O/W			15
double-layer TiO <sub>2</sub> -based mesh				5	95	16
TiO <sub>2</sub> /Co <sub>3</sub> O <sub>4</sub> /graphene oxide composite membrane	67.4	>99.5	O/W	10	96.5	17
PNL		96–99		20		18
MAC				5	95 $\pm$ 1	19
PVDF/PDA/PEI	233	>85	O/W	3		35
P(AN-MA)	4341 (0.02 bar)		O/W	10		36
iPP	1108 (0.09 MPa)		W/O	20		37
PK/PVA-NYL	420 (0.1 bar)		O/W			38
PES/SiO <sub>2</sub> -g-PMMA	143.3	98	O/W			39
PAI (HFPS)	440	99.9	O/W	18		40
PES/SPSf	858		O/W			41
PES/SPSf/GO	816.9		O/W			42
PES/SPSf/TiO <sub>2</sub>	555.2 (1.0 bar)		O/W			43
AE2311@SMA/PVDF		99	O/W	10		44
P(MMA-co-GMA)/PEI/PVDF	90	99.3	O/W	10		45
PVDF-PDMS-PEG	1009 (1 bar)	99	O/W	10		46
zwitterionic PVDF blending membrane	6350	91	O/W			47
PVDF-TiO <sub>2</sub>	400	99.7	O/W	5		48
PDA/PVDF/MWCNT	1282.5	90	O/W	6		49
NiCo-LDH/PVDF	600	99.5	O/W	10		50
Ag/EGCG-PVDF	735	95.4	O/W	5		51

compression on the separation capability of six CSC-18 balls for the O/W emulsion, the six CSC-18 balls with compression rates of 56, 63, and 72% were tested (Figure 6a–f). To prepare the emulsion, a surfactant (span 80) was used to stabilize a mixture of soybean oil and water. Two emulsions were prepared, each containing droplets with a wide range of sizes (10.6–149  $\mu$ m for the first emulsion with a transmittance of 15% and 7–63.8  $\mu$ m for the second emulsion with a transmittance of 5%) (Figure 6a,d). In both cases, emulsions with a size of 20  $\mu$ m or less account for more than 50% (insets of Figure 6a,d). The emulsion separation efficiencies were determined by calculating the variance in the absorbance of the emulsion solution before and after filtration through the CSC balls. The emulsion separation efficiencies of the six CSC-18 balls with compression rates of 56, 63, and 72% were found to be 95.8, 91.1, and 77.5%, respectively, for the first emulsion with a transmittance of 15% (yellow bars, Figure 6g). As a result of filtering the emulsion solution through these balls, the emulsion color became diluted and transparent (Figure 6b,c). Contrary to our expectations, the six CSC-18 balls with the lowest compression rate, despite having the largest pore size, exhibited the highest emulsion separation efficiency (Figure 6g). Conversely, the six CSC-18 balls with the highest compression rate, which had the smallest pore size, displayed the lowest emulsion separation efficiency (Figure 6g). This suggests that the small pores of the balls caused the large emulsion droplets to break down into smaller droplets. Thus, to remove large emulsion droplets (10.6–149  $\mu$ m) with a transmittance of 15%, it is more effective to use CSC-18 balls with larger pores (50–260  $\mu$ m, compression rate 56%) rather than the smaller ones (32–85  $\mu$ m, compression rate 72%). The emulsion separation efficiencies of six CSC-18 balls with

compression rates of 56, 63, and 72% were determined for the second emulsion, which had a transmittance of 5% (ice blue bars, Figure 6g). After the emulsion solution was filtered, the emulsion color became diluted and transparent (Figure 6e,f). Due to their higher concentration and smaller droplet size of the O/W emulsion, the six CSC-18 balls with compression rates of 56, 63, and 72% exhibited lower separation efficiencies in the emulsion with a transmittance of 5% compared to that with 15% (ice blue bars, Figure 6g). However, the results showed that the separation efficiencies were 64.8, 78.2, and 86.5%, respectively, which was in contrast to the trend observed for the emulsion with a transmittance of 15% (ice blue bars, Figure 6g). The six CSC-18 balls with the highest compression rate, which had the smallest pore size, exhibited the highest emulsion separation efficiency. Given the results, it can be concluded that for effective removal of small emulsion droplets ranging from 7 to 63.8  $\mu$ m, CSC-18 balls with smaller pores (32–85  $\mu$ m) and a higher compression rate (72%) should be used instead of larger pore sizes (50–260  $\mu$ m) with a lower compression rate (56%). In summary, for efficient elimination of small and large emulsion droplets with transmittances of 5 and 15%, respectively, it is recommended to employ CSC-18 balls with higher compression rates (72%) for small droplets and lower compression rates (56%) for large droplets. These findings indicate that the determination of the CSC-18 ball pore size should be based on the size of emulsions. The compressible nature of CSC-18 balls allows for easy control of the pore size, facilitating the effective removal of emulsions of different sizes. The flux of CSC-18 balls with compression rates of 56, 63, and 72% was also evaluated for O/W emulsions with transmittances of 5 and 15%. The experimental results demonstrated that the fluxes for the



**Figure 7.** (a) Purification setup for aqueous pollutants (MO) separated from the O/W emulsion containing MO using six CSC-18 balls. Optical microscopy images (b) before and (c) after filtration, with corresponding insets. (d) Decomposition efficiencies and emulsion separation efficiencies of MO catalyzed and separated by six CSC-18 balls up to the 10th cycle. Optical microscopy images (e) before and (f) after filtration of the O/W emulsion containing MB, with corresponding insets. (g) Decomposition efficiencies and emulsion separation efficiencies of MB catalyzed and separated by six CSC-18 balls up to the 10th cycle.

emulsion with a transmittance of 15% were 8610, 5941, and 2845 L/m<sup>2</sup> h, respectively (gray bars, Figure 6h). These fluxes decreased to 7789, 5208, and 2452 L/m<sup>2</sup> h for the emulsion with a transmittance of 5% (dark gray bars, Figure 6h). Despite the high concentrations of emulsions (transmittances of 5 and 15%), the CSC-18 balls exhibited high fluxes ranging from 2452 to 8610 L/m<sup>2</sup> h. The emulsion separation efficiency of CSC balls was measured to be in the range of 95.8–86.5%, which is slightly lower or comparable to previously reported values (Table 1). However, the CSC balls demonstrated exceptional flux performance, surpassing the values reported in previous studies (Table 1). Our CSC balls possess larger pore sizes compared with previously reported polymer membranes

(Table 1), which contributes to their high flux capability. However, these CSC balls are stacked in a multistructure arrangement, resulting in an increased path length for the emulsion solution. This longer path length enhances the separation efficiency of the system. Furthermore, the control of flux can be achieved by adjusting the compression rates of CSC balls. This flexibility allows for the effective utilization of CSC balls in various application fields that require different flux requirements. The catalytic efficiency of the CSC balls was determined to be 99.1%, surpassing the previously reported values (Table 1).

**3.8. Feasibility Test of Purifying Aqueous Pollutants during the O/W Separation.** In order to explore the

feasibility of purifying aqueous pollutants during the O/W separation, we prepared an emulsion consisting of a blend of soybean oil, surfactant (span 80), and water (MO or MB). For the test, we utilized the six CSC-18 balls with the highest and lowest compression rates, which corresponded to the smallest and largest pore sizes, respectively. The six CSC-18 balls with the lowest compression rate were used to remove large emulsion containing MO, while those with the highest compression rate were used for removal of small emulsion containing MB. Figure 7a shows the purification process for aqueous pollutants that are separated from the O (soybean oil) and W (aqueous MO solution) mixture using six CSC-18 balls. When the large emulsion was passed through the six CSC-18 balls with the lowest compression rate, the aqueous MO solution filtered quickly into a beaker below, leaving soybean oil droplets atop the same six CSC-18 balls. After the filtration, the O/W emulsion changed from yellow to transparent, and the filtered solution in the beaker no longer contained oil droplets ranging from 8.5 to 152  $\mu\text{m}$  in size (Figure 7b,c). The six CSC-18 balls with the lowest compression rate exhibited a catalytic activity of 99.1% and an emulsion separation efficiency of 91.5% up to 10 cycles when tested simultaneously (Figure 7d). These values were found to be comparable to or lower than those obtained in the catalytic test of an aqueous MO solution (99.2%) or the separation test of an O/W emulsion (95.8%), respectively (Figures 7d, 5f, and 6g). The observed phenomenon was also observed in the six CSC-18 balls with the highest compression rate when removing a small emulsion containing MB (Figure 7e,f). The six CSC-18 balls exhibited a catalytic activity and an emulsion separation efficiency of 97.9 and 76.8%, respectively, up to 10 cycles when tested simultaneously (Figure 7g).

These values were lower than or comparable to those obtained in the catalytic and separation tests of aqueous MB solution (99.9%) or O/W emulsion (76.5%), respectively (Figures 5f and 6g). These results suggest that there is no significant difference in performance between conducting catalytic and separation tests simultaneously versus conducting a catalytic test alone or separation test alone. Our CSC-18 balls with controllable distance between the catalysts exhibited exceptional catalytic performances up to 10 cycles in the process of oil/water separation, effectively demonstrating simultaneous separation and purification of emulsions and aqueous pollutants.

#### 4. CONCLUSIONS

CSC-18 balls were initially synthesized by physically etching a sponge, followed by the synthesis of three types of metal NPs with a higher content (18%). These negatively charged CSC-18 balls exhibited enhanced efficiency in the degradation of small-sized dyes such as MB, MO, and 4-NP, irrespective of the charge of the pollutant [MB(+) > MO(-) > 4-NP(-) > CR(-) > R6G(+)]. By synthesizing Ag-Pt-Pd catalysts within the sponge ball's skeleton, it became possible to control the distance between the catalysts by adjusting the compression rates of the CSC-18 ball. Properly dispersing the catalyst, instead of concentrating it in a single location, and enabling the reactant to encounter and react with the catalyst in a sequential manner can significantly boost the efficiency of the catalyst for larger sized dyes. However, concentrating the catalyst results in greater efficiency, especially for smaller sized dyes, compared to when it is dispersed. To address different emulsion droplet sizes, it is recommended to utilize CSC-18

balls with smaller and larger pore sizes for the elimination of small and large droplets, respectively. Our approach provides precise control over the pore size and catalyst distance by adjusting the compression rates of the sponge, enabling the effective removal of emulsions of various sizes, and enhancing the decomposition efficiency. The control of flux can also be achieved by adjusting the compression rates of CSC balls. Furthermore, our compressible CSC-18 balls demonstrated exceptional catalytic performance in the oil/water separation process, showcasing their capability for simultaneous separation and purification of emulsions and aqueous pollutants.

#### ■ ASSOCIATED CONTENT

##### Supporting Information

The Supporting Information is available free of charge at <https://pubs.acs.org/doi/10.1021/acsomega.3c05776>.

WCA data of the CSC ball; UV-visible absorption spectra of deionized water filtered through six CSC-18 balls over a total of 10 cycles; and chemical structures and reductive degradation (or conversion) mechanisms of five types of dyes including MO, MB, CR, R6G, and 4-NP (PDF)

#### ■ AUTHOR INFORMATION

##### Corresponding Author

Won San Choi – Department of Chemical and Biological Engineering, Hanbat National University, Yuseong-gu, Daejeon 305-719, Republic of Korea; [orcid.org/0000-0003-4546-0732](https://orcid.org/0000-0003-4546-0732); Email: [choiws@hanbat.ac.kr](mailto:choiws@hanbat.ac.kr)

##### Authors

Hee Ju Kim – Department of Chemical and Biological Engineering, Hanbat National University, Yuseong-gu, Daejeon 305-719, Republic of Korea

Young Ju Jung – Department of Chemical and Biological Engineering, Hanbat National University, Yuseong-gu, Daejeon 305-719, Republic of Korea

Su Hyeon Son – Department of Chemical and Biological Engineering, Hanbat National University, Yuseong-gu, Daejeon 305-719, Republic of Korea

Complete contact information is available at: <https://pubs.acs.org/10.1021/acsomega.3c05776>

##### Notes

The authors declare no competing financial interest.

#### ■ ACKNOWLEDGMENTS

This research was supported by the Basic Science Research Program through the National Research Foundation of Korea (NRF) funded by the Ministry of Education (NRF-2021R111A3048257).

#### ■ REFERENCES

- (1) Pandey, J. K.; Das, P.; Manna, S. *Advances in Oil–Water Separation: A Complete Guide for Physical, Chemical, and Biochemical Processes*; Elsevier Science: Netherlands, 2022.
- (2) Bhushan, B. *Bioinspired Water Harvesting, Purification, and Oil–Water Separation*; Springer International Publishing: Germany, 2020.
- (3) Xu, Z.; Zhao, Y.; Wang, H.; Wang, X.; Lin, T. A Superamphiphobic coating with an ammonia triggered transition to superhydrophilic and superoleophobic for oilwater separation. *Angew. Chem., Int. Ed.* **2015**, *54*, 4527–4530.

- (4) Choi, J. H.; Jung, Y. J.; Kim, H. J.; Seo, Y. J.; Choi, W. S. A Janus branch filter for washing machines: Simultaneous removal of microplastics and surfactants. *Chemosphere* **2023**, *331*, 138741.
- (5) Wang, Y.; Shi, Y.; Pan, L.; Yang, M.; Peng, L.; Zong, S.; Shi, Y.; Yu, G. Multifunctional superhydrophobic surfaces templated from innately microstructured hydrogel matrix. *Nano Lett.* **2014**, *14*, 4803–4809.
- (6) Chen, Y.; Li, F.; Cao, W.; Li, T. Preparation of recyclable CdS photocatalytic and superhydrophobic films with photostability by using a screen-printing technique. *J. Mater. Chem. A* **2015**, *3*, 16934–16940.
- (7) Seo, Y. J.; Han, N.; Kim, H. J.; Choi, J. H.; Koo, H. Y.; Yu, C.; Choi, W. S. A scoop net equipped with an underwater anti-oil-fouling filter for fast cleanup of low-sulfur fuel at low temperature. *J. Environ. Chem. Eng.* **2022**, *10*, 108826.
- (8) Crick, C. R.; Gibbins, J. A.; Parkin, I. P. Superhydrophobic polymer-coated copper mesh; membranes for highly efficient oil-water separation. *J. Mater. Chem. A* **2013**, *1*, 5943–5948.
- (9) Ruan, C.; Ai, K.; Li, X.; Lu, L. A superhydrophobic sponge with excellent absorbency and flame retardancy. *Angew. Chem., Int. Ed.* **2014**, *53*, 5556–5560.
- (10) Xiao, Z.; Zhang, M.; Fan, W.; Qian, Y.; Yang, Z.; Xu, B.; Kang, Z.; Wang, R.; Sun, D. Highly efficient oil/water separation and trace organic contaminants removal based on superhydrophobic conjugated microporous polymer coated devices. *Chem. Eng. J.* **2017**, *326*, 640–646.
- (11) Gao, J.; Huang, X.; Xue, H.; Tang, L.; Li, R. K. Y. Facile preparation of hybrid microspheres for super-hydrophobic coating and oil-water separation. *Chem. Eng. J.* **2017**, *326*, 443–453.
- (12) Li, J.-J.; Zhou, Y.-N.; Luo, Z.-H. Mussel-inspired V-shaped copolymer coating for intelligent oil/water separation. *Chem. Eng. J.* **2017**, *322*, 693–701.
- (13) Fu, W.; Liu, Y.; Liu, J.; Zhang, B.; Cheng, J.; Du, R.; Sun, M.; Zhao, Y.; Chen, L. A TiO<sub>2</sub> modified whisker mullite hollow fiber ceramic membrane for high-efficiency oil/water emulsions separation. *J. Eur. Ceram. Soc.* **2023**, *43*, 4451–4461.
- (14) Yan, X.; Wang, Y.; Huang, Z.; Gao, Z.; Mao, X.; Kipper, M. J.; Huang, L.; Tang, J. Janus Polyacrylonitrile/Carbon Nanotube Nanofiber Membranes for Oil/Water Separation. *ACS Appl. Nano Mater.* **2023**, *6*, 4511–4521.
- (15) Zhang, H.-R.; Ma, W.-X.; Han, X.-Y.; Chen, G.-E.; Xu, Z.-L. Intelligent pH-responsive PMMA membrane with reversible wettability for controllable oil/water and emulsion separation. *Appl. Surf. Sci.* **2023**, *615*, 156392.
- (16) Gao, C.; Sun, Z.; Li, K.; Chen, Y.; Cao, Y.; Zhang, S.; Feng, L. Integrated oil separation and water purification by a double-layer TiO<sub>2</sub>-based mesh. *Energy Environ. Sci.* **2013**, *6*, 1147–1151.
- (17) Bao, Z.; Chen, D.; Li, N.; Xu, Q.; Li, H.; He, J.; Lu, J. Superamphiphilic and underwater superoleophobic membrane for oil/water emulsion separation and organic dye degradation. *J. Membr. Sci.* **2020**, *598*, 117804.
- (18) Boakye-Ansah, S.; Lim, Y. T.; Lee, H. J.; San Choi, W. Structure-Controllable Superhydrophobic Cu Meshes for Effective Separation of Oils with Different Viscosities and Aqueous Pollutant Purification. *RSC Adv.* **2016**, *6*, 17642–17650.
- (19) Kwon Kaang, B.; Han, N.; Jang, W.; Young Koo, H.; Boo Lee, Y.; San Choi, W. Crossover magnetic amphiprotic catalysts for oil/water separation, the purification of aqueous and non-aqueous pollutants, and organic synthesis. *Chem. Eng. J.* **2018**, *331*, 290–299.
- (20) Zhang, N.; Yang, X.; Wang, Y.; Qi, Y.; Zhang, Y.; Luo, J.; Cui, P.; Jiang, W. A review on oil/water emulsion separation membrane material. *J. Environ. Chem. Eng.* **2022**, *10*, 107257.
- (21) Chen, C.; Weng, D.; Mahmood, A.; Chen, S.; Wang, J. Separation mechanism and construction of surfaces with special wettability for oil/water separation. *ACS Appl. Mater. Interfaces* **2019**, *11*, 11006–11027.
- (22) Tanis-Kanbur, M. B.; Velioğlu, S.; Tanudjaja, H.; Hu, X.; Chew, J. Understanding membrane fouling by oil-in-water emulsion via experiments and molecular dynamics simulations. *J. Membr. Sci.* **2018**, *566*, 140–150.
- (23) Kwon, G.; Kota, A.; Li, Y.; Sohani, A.; Mabry, J.; Tuteja, A. On-demand separation of oil-water mixtures. *Adv. Mater.* **2012**, *24*, 3666–3671.
- (24) Ma, H.-Y.; Hu, Y.-N.; Yang, H.; Zhu, L.-J.; Wang, G.; Zeng, Z.-X.; Wang, L.-H. In situ mussel-inspired Janus membranes using catechol and polyethyleneimine as the additives for highly efficient oil/water emulsions separation. *Sep. Purif. Technol.* **2021**, *262*, 118310.
- (25) Tseng, H.; Wu, J.; Lin, Y.; Zhuang, G. Superoleophilic and superhydrophobic carbon membranes for high quantity and quality separation of trace water-in-oil emulsions. *J. Membr. Sci.* **2018**, *559*, 148–158.
- (26) Chang, Q.; Zhou, J.; Wang, Y.; Liang, J.; Zhang, X.; Cerneaux, S.; Wang, X.; Zhu, Z.; Dong, Y. Application of ceramic microfiltration membrane modified by nano-TiO<sub>2</sub> coating in separation of a stable oil-in-water emulsion. *J. Membr. Sci.* **2014**, *456*, 128–133.
- (27) Cheng, Z.; Wang, B.; Lai, H.; Liu, P.; Zhang, D.; Tian, D.; Liu, H.; Yu, X.; Sun, B.; Sun, K. Janus copper mesh film with unidirectional water transportation ability toward high efficiency oil/water separation. *Chem.—Asian J.* **2017**, *12*, 2085–2092.
- (28) Jiang, G.; Ge, J.; Jia, Y.; Ye, X.; Jin, L.; Zhang, J.; Zhao, Z.; Yang, G.; Xue, L.; Xie, S. Coaxial electrospun nanofibrous aerogels for effective removal of oils and separation of water-in-oil emulsions. *Sep. Purif. Technol.* **2021**, *270*, 118740.
- (29) Wang, Y.; Zhou, G.; Yan, Y.; Shao, B.; Hou, J. Construction of natural loofah/poly(vinylidene fluoride) core-shell electrospun nanofibers via a controllable Janus nozzle for switchable oil-water separation. *ACS Appl. Mater. Interfaces* **2020**, *12*, 51917–51926.
- (30) Sha, Y.; Mathew, I.; Cui, Q.; Clay, M.; Gao, F.; Zhang, X. J.; Gu, Z. Rapid degradation of azo dye methyl orange using hollow cobalt nanoparticles. *Chemosphere* **2016**, *144*, 1530–1535.
- (31) Gu, J.; Kan, S.; Shen, Q.; Kan, J. Effects of sulfanilic acid and anthranilic acid on electrochemical stability of polyaniline. *Int. J. Electrochem. Sci.* **2014**, *9*, 6858–6869.
- (32) Ornelas, C.; Ruiz, J.; Salmon, L.; Astruc, D. Sulphonated “Click” Dendrimer-Stabilized Palladium Nanoparticles as Highly Efficient Catalysts for Olefin Hydrogenation and Suzuki Coupling Reactions Under Ambient Conditions in Aqueous Media. *Adv. Synth. Catal.* **2008**, *350*, 837–845.
- (33) Liu, X. L.; Yang, X.; Xin, H. Y.; Tang, X. P.; Weng, L. J.; Han, Y. Y.; Geng, D. Eco-friendly fabrication of Au/Fe<sub>3</sub>O<sub>4</sub>-chitosan composites for catalytic reduction of methyl orange. *Dig. J. Nanomater. Biostructures* **2016**, *11*, 337–348.
- (34) Saxe, J. P.; Lubenow, B. L.; Chiu, P. C.; Huang, C. P.; Cha, D. K. Enhanced biodegradation of azo dyes using an integrated elemental iron-activated sludge system: I, Evaluation of system performance. *Water Environ. Res.* **2006**, *78*, 19–25.
- (35) Xiong, Z.; He, Z.; Mahmud, S.; Yang, Y.; Zhou, L.; Hu, C.; Zhao, S. Simple amphoteric charge strategy to reinforce superhydrophilic polyvinylidene fluoride membrane for highly efficient separation of various surfactant-stabilized oil-in-water emulsions. *ACS Appl. Mater. Interfaces* **2020**, *12*, 47018–47028.
- (36) Tan, L.; Han, N.; Qian, Y.; Zhang, H.; Gao, H.; Zhang, L.; Zhang, X. Superhydrophilic and underwater superoleophobic poly(acrylonitrile-co-methyl acrylate) membrane for highly efficient separation of oil-in-water emulsions. *J. Membr. Sci.* **2018**, *564*, 712–721.
- (37) Sun, Y.; Yang, Z.; Li, L.; Wang, Z.; Sun, Q. Facile preparation of isotactic polypropylene microporous membranes with bioinspired hierarchical morphology for nano-scale water-in-oil emulsion separation. *J. Membr. Sci.* **2019**, *581*, 224–235.
- (38) Zhang, L.; Cheng, L.; Wu, H.; Yoshioka, T.; Matsuyama, H. One-step fabrication of robust and anti-oil-fouling aliphatic polyketone composite membranes for sustainable and efficient filtration of oil-in-water emulsions. *J. Mater. Chem. A* **2018**, *6*, 24641–24650.

- (39) Khodadousti, S.; Zokaee Ashtiani, F.; Karimi, M.; Fouladitajar, A. Preparation and characterization of novel PES-(SiO<sub>2</sub>-g-PmAA) membranes with antifouling and hydrophilic properties for separation of oil-in-water emulsions. *Polym. Adv. Technol.* **2019**, *30*, 2221–2232.
- (40) Asad, A.; Rastgar, M.; Sameoto, D.; Sadrzadeh, M. Gravity assisted super high flux microfiltration polyamide-imide membranes for oil/water emulsion separation. *J. Membr. Sci.* **2021**, *621*, 119019.
- (41) Zhang, L.; Cui, Z.; Hu, M.; Mo, Y.; Li, S.; He, B.; Li, J. Preparation of PES/SPSF blend ultrafiltration membranes with high performance via H<sub>2</sub>O-induced gelation phase separation. *J. Membr. Sci.* **2017**, *540*, 136–145.
- (42) Hu, M.; Cui, Z.; Li, J.; Zhang, L.; Mo, Y.; Dlamini, D.; Wang, H.; He, B.; Li, J.; Matsuyama, H. Ultra-low graphene oxide loading for water permeability, antifouling and antibacterial improvement of polyethersulfone/sulfonated polysulfone ultrafiltration membranes. *J. Colloid Interface Sci.* **2019**, *552*, 319–331.
- (43) Matindi, C.; Hu, M.; Kadanyo, S.; Ly, Q.; Gumbi, N.; Dlamini, D.; Li, J.; Hu, Y.; Cui, Z.; Li, J. Tailoring the morphology of polyethersulfone/sulfonated polysulfone ultrafiltration membranes for highly efficient separation of oil-in-water emulsions using TiO<sub>2</sub> nanoparticles. *J. Membr. Sci.* **2021**, *620*, 118868.
- (44) Xu, C.; Yan, F.; Wang, M.; Yan, H.; Cui, Z.; Li, J.; He, B. Fabrication of hyperbranched polyether demulsifier modified PVDF membrane for demulsification and separation of oil-in-water emulsion. *J. Membr. Sci.* **2020**, *602*, 117974.
- (45) Deng, Y.; Zhang, G.; Bai, R.; Shen, S.; Zhou, X.; Wyman, I. Fabrication of superhydrophilic and underwater superoleophobic membranes via an in situ crosslinking blend strategy for highly efficient oil/water emulsion separation. *J. Membr. Sci.* **2019**, *569*, 60–70.
- (46) Bhalani, D.; Jewrajka, S. Fouling resistant amphiphilic poly(dimethylsiloxane)-linked-poly(ethylene glycol) network on ultrafiltration poly(vinylidene fluoride) membrane and effect of spatial chain arrangement on separation of oil-water emulsions. *J. Membr. Sci.* **2019**, *583*, 278–291.
- (47) Zhu, Y.; Xie, W.; Zhang, F.; Xing, T.; Jin, J. Superhydrophilic in-situ-cross-linked zwitterionic polyelectrolyte/PVDF-blend membrane for highly efficient oil/water emulsion separation. *ACS Appl. Mater. Interfaces* **2017**, *9*, 9603–9613.
- (48) Deng, W.; Fan, T.; Li, Y. In situ biomineralization-constructed superhydrophilic and underwater superoleophobic PVDF-TiO<sub>2</sub> membranes for superior antifouling separation of oil-in-water emulsions. *J. Membr. Sci.* **2021**, *622*, 119030.
- (49) Yang, X.; He, Y.; Zeng, G.; Chen, X.; Shi, H.; Qing, D.; Li, F.; Chen, Q. Bio-inspired method for preparation of multiwall carbon nanotubes decorated superhydrophilic poly(vinylidene fluoride) membrane for oil/water emulsion separation. *Chem. Eng. J.* **2017**, *321*, 245–256.
- (50) Cui, J.; Zhou, Z.; Xie, A.; Wang, Q.; Liu, S.; Lang, J.; Li, C.; Yan, Y.; Dai, J. Facile preparation of grass-like structured NICO-LDH/PVDF composite membrane for efficient oil-water emulsion separation. *J. Membr. Sci.* **2019**, *573*, 226–233.
- (51) Zhang, N.; Yang, N.; Zhang, L.; Jiang, B.; Sun, Y.; Ma, J.; Cheng, K.; Peng, F. Facile hydrophilic modification of PVDF membrane with AG/EGCG decorated micro/nanostructural surface for efficient oil-in-water emulsion separation. *Chem. Eng. J.* **2020**, *402*, 126200.